UC Davis
UC Davis Previously Published Works

Title
Light-triggered nitric oxide release and structure transformation of peptide for enhanced intratumoral retention and sensitized photodynamic therapy

Permalink
https://escholarship.org/uc/item/5vb689pz

Authors
Jiang, Lingdong
Chen, Danyang
Jin, Zhaokui
et al.

Publication Date
2022-06-01

DOI
10.1016/j.bioactmat.2021.09.035

Peer reviewed

eScholarship.org Powered by the California Digital Library
University of California

Bioactive Materials 12 (2022) 303–313

Contents lists available at ScienceDirect

Bioactive Materials

journal homepage: www.keaipublishing.com/en/journals/bioactive-materials

Light-triggered nitric oxide release and structure transformation of peptide for enhanced intratumoral retention and sensitized photodynamic therapy

Lingdong Jiang [a,b,d], Danyang Chen [a], Zhaokui Jin [a], Chao Xia [a], Qingqing Xu [a], Mingjian Fan [a], Yunlu Dai [e], Jia Liu [c,**], Yuanpei Li [d,***], Qianjun He [a,c,*]

[a] Marshall Laboratory of Biomedical Engineering, School of Biomedical Engineering, Health Science Center, Shenzhen University, No. 1066 Xueyuan Avenue, Shenzhen, 518060, Guangdong, China
[b] Key Laboratory of Optoelectronic Devices and Systems of Ministry of Education and Guangdong Province, College of Optoelectronic Engineering, Shenzhen University, Shenzhen, 518060, Guangdong, China
[c] Central Laboratory, Longgang District People's Hospital of Shenzhen & The Third Affiliated Hospital (Provisional) of The Chinese University of Hong Kong, Shenzhen, 518172, Guangdong, China
[d] Department of Biochemistry and Molecular Medicine, UC Davis Comprehensive Cancer Center, University of California Davis, Sacramento, CA, 95817, USA
[e] Cancer Centre and Institute of Translational Medicine, Faculty of Health Sciences, University of Macau, Macau SAR, 999078, China

ARTICLE INFO

Keywords:
Nitric oxide
Photodynamic therapy
Structural transformation
Peptide
Enhanced intratumoral retention
Nanomedicine

ABSTRACT

Tumor-targeted delivery of nanomedicine is of great importance to improve therapeutic efficacy of cancer and minimize systemic side effects. Unfortunately, nowadays the targeting efficiency of nanomedicine toward tumor is still quite limited and far from clinical requirements. In this work, we develop an innovative peptide-based nanoparticle to realize light-triggered nitric oxide (NO) release and structural transformation for enhanced intratumoral retention and simultaneously sensitizing photodynamic therapy (PDT). The designed nanoparticle is self-assembled from a chimeric peptide monomer, TPP-RRRKLVFFK-Ce6, which contains a photosensitive moiety (chlorin e6, Ce6), a β-sheet-forming peptide domain (Lys-Leu-Val-Phe-Phe, KLVFF), an oligoarginine domain (RRR) as NO donor and a triphenylphosphonium (TPP) moiety for targeting mitochondria. When irradiated by light, the constructed nanoparticles undergo rapid structural transformation from nanosphere to nanorod, enabling to achieve a significantly higher intratumoral accumulation by 3.26 times compared to that without light irradiation. More importantly, the conversion of generated NO and reactive oxygen species (ROS) in a light-responsive way to peroxynitrite anions ($ONOO^-$) with higher cytotoxicity enables NO to sensitize PDT in cancer treatment. Both *in vitro* and *in vivo* studies demonstrate that NO sensitized PDT based on the well-designed transformable nanoparticles enables to eradicate tumors efficiently. The light-triggered transformable nanoplatform developed in this work provides a new strategy for enhanced intratumoral retention and improved therapeutic outcome.

1. Introduction

Nanomaterials have garnered great attention in drug delivery and improved bioavailability. The enhanced permeability and retention (EPR) effect based on leaky tumor vessels, albeit the increasing debate on the effectiveness to the heterogeneous tumor [1], is widely considered a major driving force for nanoparticles (NPs) to accumulate in tumor. Whereas due to the rapid metabolic clearance, NPs still face the inherent restriction of poor targeting efficiency (often less than 1% of injected dose) [2,3], which inevitably leads to serious side effects and even the failure of cancer treatment. In order to augment the targeting efficiency of NPs, a typical strategy is to functionalize the surface of nanomaterials with active targeting molecules (*e.g.* antibody, folic acid, galactose, transferrin, integrin receptor, *etc.*) [4]. However, intensive

Peer review under responsibility of KeAi Communications Co., Ltd.
* Corresponding author. Marshall Laboratory of Biomedical Engineering, School of Biomedical Engineering, Health Science Center, Shenzhen University, No. 1066 Xueyuan Avenue, Shenzhen, 518060, Guangdong, China.
** Corresponding author.
*** Corresponding author.
E-mail addresses: liujia870702@126.com (J. Liu), lypli@ucdavis.edu (Y. Li), nanoflower@126.com (Q. He).

https://doi.org/10.1016/j.bioactmat.2021.09.035
Received 13 August 2021; Received in revised form 14 September 2021; Accepted 23 September 2021
Available online 28 October 2021
2452-199X/© 2021 The Authors. Publishing services by Elsevier B.V. on behalf of KeAi Communications Co. Ltd. This is an open access article under the CC BY-NC-ND license (http://creativecommons.org/licenses/by-nc-nd/4.0/).

studies reveal that the improvement contributed from these targeting molecules is quite limited, and passive targeting still makes a major contribution to tumor targeting [5]. Therefore, recently much attention has been drawn to exploiting strategies that can boost the passive targeting efficiency of nanomaterials. The morphology is an important parameter of NPs that affects the tumor targeting efficiency greatly [6]. As reported previously [7], rod shape is one of the best morphologies of NPs with extraordinary retention ability, which can be uptaken more efficiently by living cells and have more restriction on the backflow to the systemic circulation, thus exhibiting superior therapeutic efficacy against cancer. However, one contradiction is that rod shape is not advantageous for NPs in blood circulation compared to their spherical counterparts. Besides, long rod-like NPs are less efficient in extravasation from the leaky tumor vessel [8]. To resolve this challenge, scientists put forward the exploitation of nanomaterials with transformable property to enhance the retention of nanomedicines in tumor tissues [9,10]. This strategy harnesses the advantages of small NPs with spherical shape in rapid influx and their transformed counterparts in prolonged retention upon appropriate stimulation. Such *in situ* structural transformation of NPs is generally designed to be responsive to the tumor microenvironment (TME). For instance, acid-triggered transformation of peptide NPs [11,12], glutathione-induced transformation of gold-silver nanocages [13], and enzyme-catalyzed or receptor-mediated transformation of nanofibers [14,15], have been reported. However, the sensitivity and responsivity of these nanomaterials to the TME are frequently weak and uncontrollable. To address this challenge, in current work we proposed a light-triggered structural transformation strategy to realize enhanced intratumoral retention and accumulation of nanomedicines by virtue of easy manipulation of light as a stimulus.

Photodynamic therapy (PDT) is highly appreciated in clinical cancer therapy owing to its unique selectivity and minimal invasiveness [16–19]. Upon specific light irradiation, photosensitizers can generate cytotoxic reactive oxygen species (ROS) to locally induce the necrosis or apoptosis of cancer cells. Since ROS has a short lifetime (shorter than 200 ns) and a limited diffusion distance (approximately 20 nm) [20,21], the PDT efficacy depends heavily on the intracellular accumulation and subcellular localization of photosensitizer. Therefore, precise delivery of photosensitizer to specific suborganelle can improve the PDT efficacy. Recently, nitric oxide (NO) as an endogenous signal molecule involved in many physiological and pathological processes [22], has been well

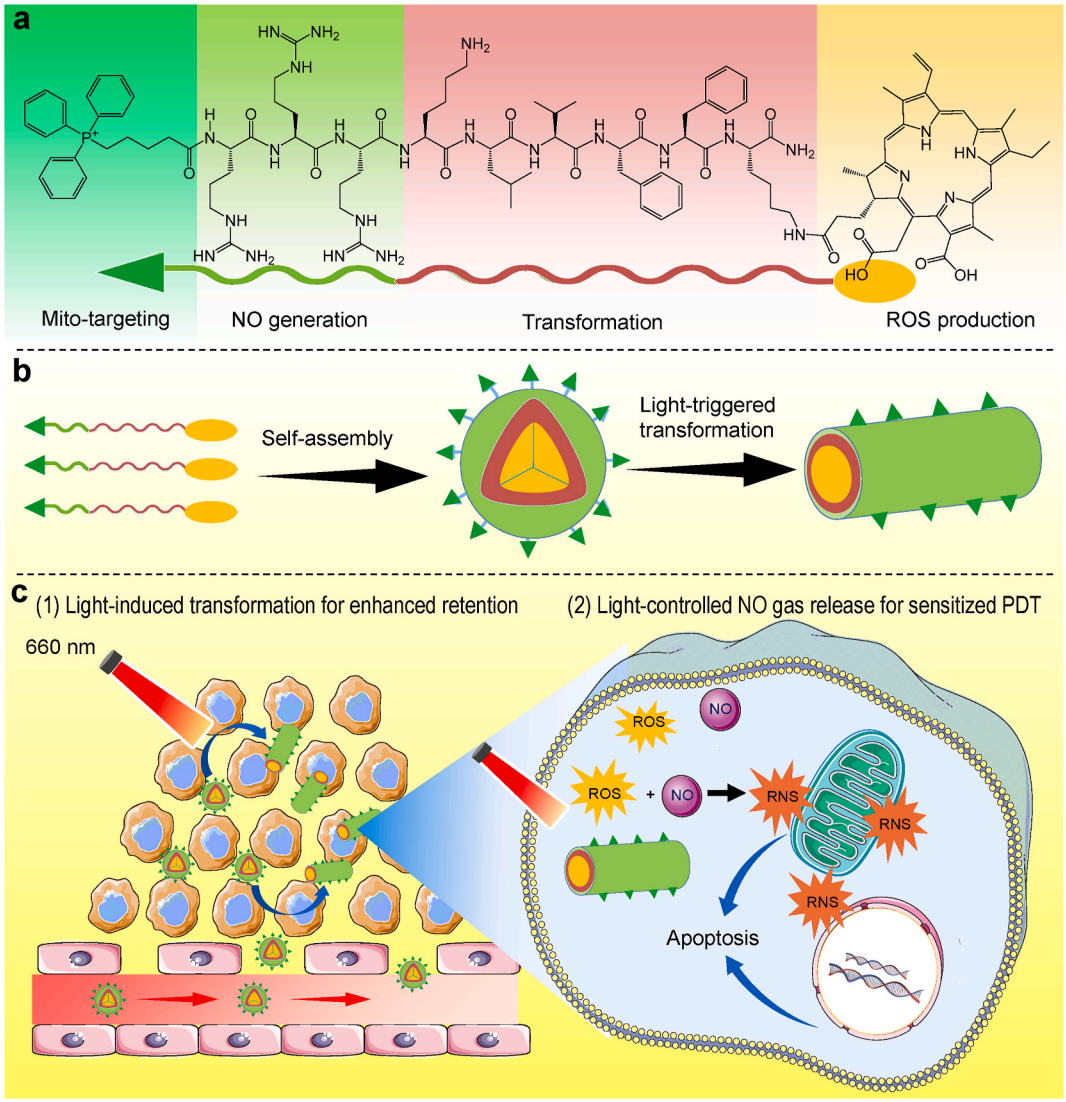

Fig. 1. Schematic illustration of the light-triggered NO generation and structural transformation of peptide-based NPs for enhanced intratumoral retention and sensitizing PDT. (a) Molecular structure of TRFC peptide monomer. (b) Schematic illustration of self-assembly and *in situ* light-triggered nanosphere−to−nanorod structural transformation of TRFC NPs. (c) Schematic illustration of structural transformation for enhanced intratumoral retention and the mechanism of NO gas sensitized PDT treatment.

reported for tumor therapy [23–26]. Owing to the excellent biocompatibility and the favorable ability of NO production under the catalysis of inducible NO synthase (iNOS) or the oxidization of ROS [27,28], L-arginine (L-Arg) as a natural amino acid, illustrated much more superiority compared to conventional N-diazeniumdiolate (NONOate)-based and S-nitrosothiols (RSNO)-based NO donors [29,30]. Given that mitochondria are the main energy source of cells and that NO is able to induce the death of cancer cells by inhibiting the energy metabolism [31,32], the endowment of nanomaterials with mitochondrial-targeting ability is potentially an excellent strategy to realize NO enhanced PDT.

In this work, we designed and synthesized a chimeric peptide by a standard solid phase peptide synthesis (SPPS) method [33], discovered its excellent self-assembly behavior and *in situ* light-triggered transformation property from nanosphere to nanorod. Fig. 1 described the molecular structure of the peptide and the therapeutic mechanism. Briefly, the transformable peptide monomer, TPP-RRRKLVFFK-Ce6, designated as TRFC, is composed of four discrete functional domains (Fig. 1a): (1) the Ce6 moiety for ROS production and fluorescence reporting, and as a hydrophobic core to form nanospheres; (2) Lys-Leu-Val-Phe-Phe (KLVFF), a domain derived from β-amyloid (Aβ) peptide [34], tending to form a β-sheet structure due to the extensive intermolecular hydrogen bonds, playing the major role in structural transformation; (3) an oligoarginine domain (RRR), as NO donor to release NO gas when oxidized by ROS; and (4) a triphenylphosphonium (TPP) moiety for mitochondrial targeting [35]. Under aqueous conditions, TRFC monomers self-assembled into spherical NPs. Upon light irradiation, the photosensitizer (Ce6) produced a plenty of ROS and induced the oxidation of oligoarginine to generate NO. The release of NO gas simultaneously drove the *in situ* nanosphere−to−nanorod transformation, facilitating the enhanced intratumoral internalization and retention (Fig. 1b). Most importantly, the further reaction between NO and ROS yielded peroxynitrite anions ($ONOO^-$) which had remarkably increased cytotoxicity [36], thereby allowing to amplify the PDT therapeutic outcome (Fig. 1c) [37,38]. Compared with routine photodynamic nanoformulations, the NPs developed in this work exhibited three main advantages, including (1) light-triggered structural transformation property to enhance intratumoral retention; (2) the chemically stable conjugation of photosensitizer and NO donor as a molecular entity to avoid drug loading process, thereby addressing the concern of drug leakage during transportation, and (3) the NO gas sensitized PDT treatment enabling to achieve improved therapeutic outcome.

2. Experimental section

2.1. Synthesis and characterization of peptide monomers

Peptide monomers were prepared *via* a SPPS method on rink amide resin using a peptide synthesizer. For the synthesis of TRF monomer, 1 g of rink amide resin (containing ~0.6 mmol amine groups), Fmoc-Lys (Dde)-OH (3.6 mmol), Fmoc-Phe-OH (7.2 mmol), Fmoc-Val-OH (3.6 mmol), Fmoc-Leu-OH (3.6 mmol), Fmoc-Lys(Boc)-OH (3.6 mmol), Fmoc-Arg(Pbf)-OH (10.8 mmol) and (4-Carboxybutyl)triphenylphosphonium bromide (3.6 mmol) were dissolved in DMF separately and loaded into different glass bottles of the peptide synthesizer. *N,N′*-diisopropylcarbodiimide (DIC) and hydroxybenzotriazole (HOBt) were used as coupling reagents. Piperidine/DMF (20%, v/v) was employed to remove Fmoc group. Hydrazine hydrate/DMF (2%, v/v) was employed to remove Dde group. The TRF peptide was cleaved from the resin using a mixture solution of trifluoroacetic acid (TFA), triisopropylsilane (TIS), and H_2O in the volume ratio of 95:2.5:2.5 for 2 h. The crude product was separated from the solvent by rotary evaporation, followed by purification *via* HPLC with a C18 column by a gradient elution. For the synthesis of TRFC monomer, the synthetic process is similar to TRF monomer except that Ce6 (3.6 mmol) was coupled to the peptide before cleaved from the resin. For the synthesis of TKFC monomer, the synthetic process is similar to TRFC monomer except that Fmoc-Arg(Pbf)-OH (10.8 mmol) was replaced by Fmoc-Lys(Boc)-OH (10.8 mmol). The mass spectra of the synthesized peptides were recorded on the ABI 4700 MALDI-TOF/TOF mass spectrometer (linear mode), using 2,5-dihydroxybenzoic acid as a matrix.

2.2. Preparation and characterization of NPs

Peptide monomers (2 mg) were first dissolved in 20 μL of DSMO and then added into 980 μL of PBS (pH 7.4), followed by sonication for 1 min. The hydrodynamic size of NPs was measured by dynamic light scattering (DLS, Malvern Zetasizer Nano-ZS). The morphology and structure of NPs were characterized using scanning electron microscopy (SEM, Thermo APREO-S). The ultraviolet–visible (UV–vis) absorption spectra were measured on a UV–Vis spectrophotometer (UV-1800, Shimadzu). The fluorescence spectra were recorded on a fluorescence spectrophotometer (RF6000, Shimadzu).

2.3. NO release measurement in solution

The NO generation from TRFC NPs (100, 125, 250, 500 μM) was determined with a commercial Griess Reagent (Beyotime S0021) upon irradiated by light with a series of power densities (0.25, 0.5, 1.0 W cm^{-2}) for different time durations. The concentration of released NO was quantified according to the manufacturer's instructions. Briefly, TRFC NPs dispersed in PBS were subjected to light irradiation, and then 50 μL of supernatant was collected by centrifugation, followed by the addition of Griess reagent I (50 μL) and reagent II (50 μL). The formation of a diazo compound could be determined by the UV–vis spectrophotometer at 540 nm.

2.4. $ONOO^-$ generation measurement in solution

The $ONOO^-$ generation profile from TRFC NPs (125, 250, 500 μM) was determined with a commercial fluorescent probe BBoxiProbe® O72 (516/606 nm) upon irradiated by light with a power density (0.25 W cm^{-2}) for different time durations. The determination was according to the manufacturer's instructions. Briefly, 100 μL of TRFC NPs dispersed in PBS were subjected to light irradiation, and then 100 μL of diluted fluorescent probe was added followed by the measurement of fluorescence intensity.

2.5. Light-triggered structural transformation and intratumoral retention

Light-triggered structural transformation for intratumoral retention and accumulation of TRFC NPs was investigated by monitoring intratumoral fluorescence *via* IVIS imaging systems (PerkinElmer) in real time. The 4T1-tumor-bearing mouse model was built by subcutaneous injection of 1×10^7 4T1 cells into the hind limb of each female Balb/c mouse. When the tumor size reached approximately 100 mm^3, the mice were injected with TRFC NPs (10 mg kg^{-1}) intravenously before fluorescence imaging. For experiment groups, the tumors were irradiated with light (660 nm, 0.25 W cm^{-2}, 3 min) at 2 h or 4 h after injection with TRFC NPs, and the mice were imaged at preset time points (0.5, 2, 4, 6, 12, 24, 48 h). The mice in control group were treated in the same way as the experiment groups except for the absence of light irradiation.

2.6. Colocalization assay

4T1 cells (1×10^6) were seeded into confocal Petri dish and incubated at 37 °C. After 24 h, the cells were co-incubated with TRFC NPs (40 μM) for different time durations ranging from 10 min to 4 h. Afterwards, the cells were washed twice with PBS to remove excess TRFC NPs, followed by incubation with MitoTracker Green (Meilunbio®, China) for 30 min. Cells were observed using confocal laser scanning

microscopy (CLSM, ZEISS-LSM880) to evaluate the subcellular localization of TRFC NPs. The corresponding Pearson correlation coefficient was calculated with ImageJ software.

2.7. Measurement of intracellular ATP level

An ATP assay kit (Beyotime S0026) was employed for the measurement of intracellular ATP level. Briefly, 4T1 cells (1×10^4) were seeded into 96-well plates and incubated at 37 °C for 24 h. The culture media were replaced with fresh ones containing 40 μM of TFR, TKFC and TRFC NPs, respectively, followed with light irradiation (660 nm, 0.25 W cm^{-2}, 3 min). After 2 h, 4T1 cells were lysed and the supernatant was immediately collected by centrifugation, followed by the detection of ATP levels using an ATP assay kit.

2.8. Measurement of ROS, NO and $ONOO^-$ in cellular and tumoral level

For the measurement of intracellular ROS level change, a fluorescent probe DCF-DA (488/525 nm) was employed. Briefly, 4T1 cells (1×10^4) were seeded into 96-well plates and incubated at 37 °C for 24 h before the addition of fresh culture medium containing the TRFC NPs at a final concentration of 40 μM. After incubation for another 4 h, the cells were washed twice with PBS to remove excess TRFC NPs, and incubated with DCF-DA dissolved in serum-free medium at a final concentration of 10 μM for 20 min. After that, the cells were irradiated by light (660 nm, 0.25 W cm^{-2}, 3 min) and the fluorescence signal was recorded using a microplate reader (Bio-Tek). Wells without light irradiation served as negative control, and the wells without incubation with NPs served as the blank control (background). Experiment groups extracted the background group to obtain the change of intracellular ROS level. For the measurement of intracellular NO and $ONOO^-$ levels, the cells were treated in the same way as the measurement of ROS level except that the fluorescent probes DAF-FM DA (495/515 nm) and BBoxiProbe® O72 (516/606 nm) were employed to determine the change of intracellular NO and $ONOO^-$, respectively. For the measurement of intratumoral NO and $ONOO^-$ levels, the 4T1 tumor-bearing mice were intravenously injected with TRFC NPs (10 mg kg^{-1}) followed by light irradiation at 4 h and 6 h post-injection, and then the tumors were excised and smashed with RIPA buffer, and then centrifuged to collect the supernatant. The NO and $ONOO^-$ levels were also evaluated using the DAF-FM DA (495/515 nm) and BBoxiProbe® O72 (516/606 nm) probes, respectively. Tumors without light irradiation were employed as control.

2.9. In vitro cytotoxicity and cellular apoptosis assay

4T1, MCF-7 and B16 cells (1×10^4 cells/well) were seeded into 96-well culture plates. After incubation at 37 °C for 24 h, the cells were co-incubated with TRF, TKFC or TRFC NPs at various final concentrations of 2.5–40 μM for 4 h, and then the cells were washed twice by PBS and fresh culture medium was added before light irradiation (660 nm, 0.25 W cm^{-2}) for 1 or 3 min. The cells were then incubated at 37 °C for 24 h and a standard CCK-8 kit was used to determine cell viabilities. The absorbance at 450 nm was measured using the microplate reader. Cells without light irradiation served as control. For LIVE/DEAD assay, 4T1 cells (1×10^6 cells/well) were seeded into 6-well culture plates and incubated for 24 h. The cells were co-incubated with TRF, TKFC or TRFC NPs at a final concentration of 40 μM for another 4 h. The cells were then washed twice with PBS before exposed to light irradiation (660 nm, 0.25 W cm^{-2}, 3 min). After that, Calcein AM and PI were utilized to stain living and dead cells, respectively. The stained cells were observed by fluorescence inverted microscopy (Nikon TS2-S-SM). For flow cytometry analysis, Annexin V-FITC/PI apoptosis detection kit was used. Briefly, 4T1 cells (1×10^6) were seeded into 6-well plates and incubated for 24 h. After that, the culture medium was replaced with a fresh one containing TRF, TKFC or TRFC NPs at a final concentration of 40 μM and cells were cultured for another 4 h. Subsequently, the cells were washed twice with PBS and then exposed to light irradiation (660 nm, 0.25 W cm^{-2}, 3 min) or not. After incubation for 1 h, the cells were collected and then stained with Annexin V-FITC/PI before analyzed by flow cytometry (BD FACSCalibur, USA).

2.10. In vivo biodistribution

4T1 tumor-bearing mice were employed to investigate the biodistribution of TRFC NPs *in vivo*. TRFC NPs (10 mg kg^{-1}) were intravenously injected into the mice ($n = 3$) *via* the tail vein. The mice were sacrificed at preset time points post-injection. The heart, liver, spleen, lung, kidney, and tumor were exfoliated and imaged using IVIS Spectrum imaging system.

2.11. In vivo therapeutic effects evaluation

All healthy female Balb/c mice (4 weeks old) were purchased from Yancheng Biotechnology Co., Ltd (Guangzhou, China) and all the *in vivo* experiments were strictly in compliance with the guidelines of the Animal Care and Use Committee of Shenzhen University. 4T1 tumor-bearing mice model was built by subcutaneous injection of 1×10^7 4T1 cells into the hind limb of each mouse. After the tumor volume of mice reached approximately 100 mm^3, the treatment was performed (designed as Day 0). These mice were randomized into eight groups ($n = 6$ for each independent group). For the control groups, mice were intravenously injected with 100 μL of TRF, TKFC, TRFC NPs (10 mg kg^{-1}) or PBS on Day 0 and Day 9, respectively; for the groups with light irradiation, mice were intravenously injected with 100 μL of TRF, TKFC, TRFC NPs (10 mg kg^{-1}) or PBS on Day 0 and Day 9, and the light irradiation (660 nm, 3 min, 0.25 W cm^{-2}) was carried out on Day 0 (at 4 h and 6 h post-injection), Day 1 (at 24 h post-injection), Day 9 (at 4 h and 6 h post-injection) and Day 10 (at 24 h post-injection). The body weight and tumor volume ($width^2 \times length \times 0.5$) of each mouse were measured regularly.

2.12. Histological staining analysis

At the end of treatment, all tumors were collected and fixed in a 4% paraformaldehyde solution for H&E, Ki67, TUNEL, Iba1, and CD31 staining assay to evaluate the therapeutic effect. The main organs (heart, liver, spleen, lung, and kidney) in each group were harvested for H&E assay to evaluate the toxicity of the materials.

2.13. In vivo biocompatibility assay

TRFC NPs were intravenously administrated into healthy BALB/c mice ($n = 3$) at different dosages. After one week, the standard biochemistry test was conducted to evaluate the liver/kidney functions related indicators including alkaline phosphatase ALP, alanine transaminase ALT, aspartate transaminase AST, creatinine CREA and blood urea nitrogen BUN. The blood panel parameters including white blood cells WBC, red blood cells RBC, haemoglobin HGB, mean corpuscular haemoglobin concentration MCHC, lymphocyte LYM, haematocrit HCT, mean corpuscular volume MCV, mean corpuscular haemoglobin MCH, and red blood cell distribution width-standard deviation RDW-SD were also evaluated.

2.14. Statistical analysis

The data were presented as mean ± standard deviation (SD). Differences between groups were tested for statistical significance with the two-tailed Student's *t*-test. Differences were considered statistically significant at a level of $*P < 0.05$, $**P < 0.01$, $***P < 0.001$.

3. Results and discussion

3.1. Synthesis, characterization and light responsiveness of TRFC NPs

Peptide monomer TPP-RRRKLVFFK-Ce6 (TRFC) and the control peptide monomers TPP-RRRKLVFFK (TRF, lack of the photosensitizer Ce6 domain) and TPP-KKKKLVFFK-Ce6 (TKFC, replacement of NO donor domain with oligolysine) were prepared through a standard Fmoc solid phase peptide synthesis (SPPS) method. MALDI-TOF confirmed the validity of the molecular weight of synthesized peptide monomers (Fig. S1–S3, Supporting Information). The peaks at *m/z* 2172, *m/z* 1594, and *m/z* 2088 belong to TRFC, TRF and TKFC monomer, respectively, confirming the successful synthesis of the peptide monomers. The UV–visible and fluorescence spectra were also employed for structure confirmation (Fig. S4 and Fig. S5, Supporting Information). TRFC showed the similar absorption peaks to free Ce6, one at around 400 nm and the other at around 650 nm. In terms of fluorescence, TRFC also exhibited the similar emission spectra to Ce6.

After confirmed on the molecular structure of peptide monomers, TRFC, TRF and TKFC NPs were prepared from the corresponding peptide monomers *via* a nanoprecipitation method. SEM analysis was conducted to investigate the self-assembly and light triggered transformation behavior of NPs. As revealed from SEM images, without light treatment, TRFC NPs exhibited a well-defined and uniform spherical morphology with diameter at around 120 nm (Fig. 2a). After only 1 min of light irradiation (660 nm, 0.25 W cm^{-2}), a great number of spherical NPs transformed into rod-like ones (Fig. 2b). With the elongation of irradiation time to 3 min, almost all the spherical NPs transformed into nanorod (Fig. 2c), indicating that the structural transformation was highly responsive to light irradiation, thereby enabling to precisely control the transformation behavior of TRFC NPs on demand during treatment. DLS analysis was further conducted to monitor the hydrodynamic particle size change of NPs in real time (Fig. 2d). It revealed that without light irradiation, TRFC NPs showed a hydrodynamic size of around 140 nm with a narrow size distribution. After 1 min of light irradiation, TRFC NPs showed a bigger hydrodynamic particle size and a wider size distribution. With the elongation of light irradiation to 3 min, the particle size achieved around 420 nm. In order to gain a better insight of the structural transformation mechanism, TRFC NPs, TKFC NPs (control particle, replacement of oligoarginine with oligolysine) and TRF NPs (control particle, lack of Ce6 moiety) were also subjected to light irradiation and analyzed by DLS and SEM (Fig. S6, Supporting Information). The results revealed that the TKFC NPs were able to self-assemble into spherical morphology in solution, but no transformation was observed irrespective of light irradiation, which demonstrated that ROS generation alone could not overcome the hydrophobic force of Ce6 moiety and fail to induce the structural transformation. On the other hand, in the absence of the hydrophobic Ce6 domain, TRF NPs tended to self-assemble into rod-like morphology directly in solution, probably resulting from the intermolecular hydrogen bonds of KLVFF domain that dominated the self-assembly behavior and led to the formation of a β-sheet structure. These results jointly elucidated that the rapid sphere–to–rod structural transformation property of TRFC NPs relied on both the hydrophobic photosensitizer Ce6 moiety and the oligoarginine domain (as NO donor), which involved in a cascade reaction of ROS generation and the subsequent burst release of NO gas upon triggered by light irradiation (Fig. S7, Supporting Information). The release of NO gas disturbed the metastable nanospheric structure and drove the formation of nanorod-like morphology. In order to investigate the NO gas release profile of TRFC NPs, a standard Greiss reagent test kit was employed to quantify the released NO gas upon triggered by light with different power densities. As demonstrated in Fig. S8 and Fig. S9 (Supporting Information), the production of NO exhibited power-density-dependent and concentration-dependent characteristics. By contrast, in the absence of light irradiation, no production of NO was detected, demonstrating the practicability of on-demand NO release by easy manipulation of light

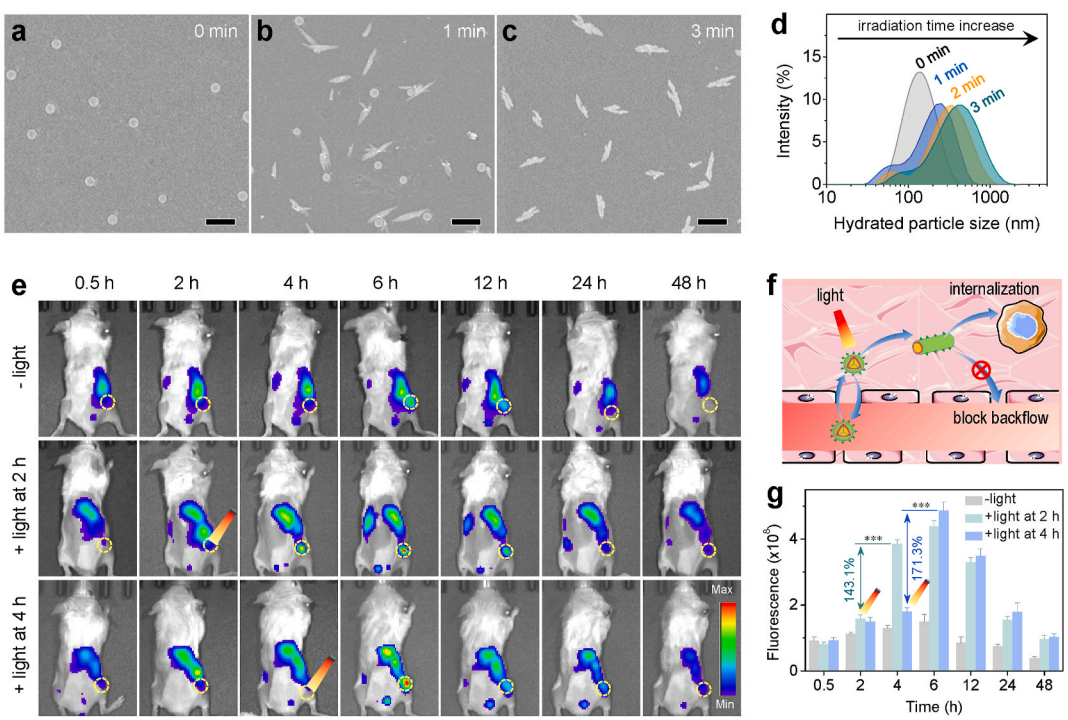

Fig. 2. Light-triggered transformation of TRFC NPs for enhanced intratumoral retention. SEM images showing the structure morphology of TRFC NPs without light irradiation (a), with 1 min (b) and 3 min (c) of light irradiation (660 nm, 0.25 W cm^{-2}), respectively. Scale bar: 500 nm. (d) The real-time monitoring of the hydrated particle size change of TRFC NPs with the elongation of irradiation time. (e) The *in vivo* real-time fluorescence imaging of 4T1 tumor-bearing mice with or without light irradiation (660 nm, 0.25 W cm^{-2}, 3 min) at 2 h or 4 h after intravenous injection of TRFC NPs. (f) Schematic illustration of transformable TRFC NPs for enhanced intratumoral retention based on improving cellular internalization and impeding backflow to bloodstream. (g) Corresponding analysis of enhanced intratumoral accumulation of TRFC NPs from fluorescence signal in (e).

irradiation. As above mentioned, further reaction between NO and ROS enabled to yield $ONOO^-$ with remarkably increased cytotoxicity, in order to validate the generation of $ONOO^-$, a fluorescent probe BBox-iProbe® O72 was used to investigate the generation profile of $ONOO^-$. As demonstrated in Fig. S10 (Supporting Information), the production of $ONOO^-$ also displayed concentration-dependent characteristics.

3.2. Intratumoral light-triggered transformation and retention performances

As well reported elsewhere, rod-like NPs can be uptaken more efficiently by living cells than their spherical counterparts, and are beneficial for their accumulation in tumor [39]. Therefore, after verification of the structural transformation property of the TRFC NPs *in vitro*, we further investigated the influence of structural transformation on their intratumoral accumulation. Owing to the existence of fluorescent Ce6 moiety in TRFC NPs, it enabled us to execute fluorescence imaging to evaluate the intratumoral accumulation behavior of NPs in the presence or absence of light irradiation. The TRFC NPs were intravenously injected into 4T1 tumor-bearing mice and their tumor targeting behaviors were monitored at preset time intervals using the IVIS imaging system. As shown in Fig. 2e, in the absence of light irradiation, TRFC NPs can mildly accumulate into tumor in a passive targeting way after intravenous injection into mice as many other nanomedicines did. The fluorescence intensity of tumor increased gradually and reached the maximum at 6 h post-injection, and then decreased with time. To investigate the effect of structural transformation on the intratumoral retention and accumulation of TRFC NPs, the tumor-bearing mice were subjected to light irradiation (660 nm, 0.25 W cm^{-2}, 3 min) at 2 h or 4 h after intravenous injection. The choice of irradiation timing was based on the accumulation profile of TRFC NPs without light intervention. The accumulation of TRFC NPs at tumor site was still relatively low at 0.5 h, whereas at 6 h the accumulation had reached the maximum level. Therefore, 2 h and 4 h post-injection of TRFC NPs were considered to be appropriate time points for light irradiation. Notably, the mice after receiving light irradiation at either 2 h or 4 h displayed a dramatic increase of intratumoral fluorescence intensity within 2 h. The mice receiving light irradiation at 2 h and 4 h displayed a fluorescence signal increase by 1.43 and 1.71 times 2 h after light irradiation, respectively. Moreover, compared with the tumor without light irradiation, remarkably stronger fluorescence signals (2.93 or 3.26 times) persisted in the light-treated tumors at 6 h (Fig. 2g). Obviously, this notable increase in fluorescence signal intensity was contributed from the sphere−to−rod structural transformation, which facilitated cellular internalization and was able to impede the backflow of spherical NPs to the systemic circulation, thereby achieving the enhancement of intratumoral retention and accumulation of NPs (Fig. 2f). Additionally, in order to gain an insight of the bio-distribution of TRFC NPs in tumor-bearing mice, TRFC NPs were intravenously injected into mice *via* tail vein and then the tumors and visceral organs (heart, liver, spleen, lung, and kidney) were collected at preset time intervals for *ex vivo* imaging and recording their corresponding fluorescence intensity. From Fig. S11 (Supporting Information), the *ex vivo* measurement of TRFC NPs in tumors indicated a similar accumulation profile as *in vivo* determined. Notably, TRFC NPs

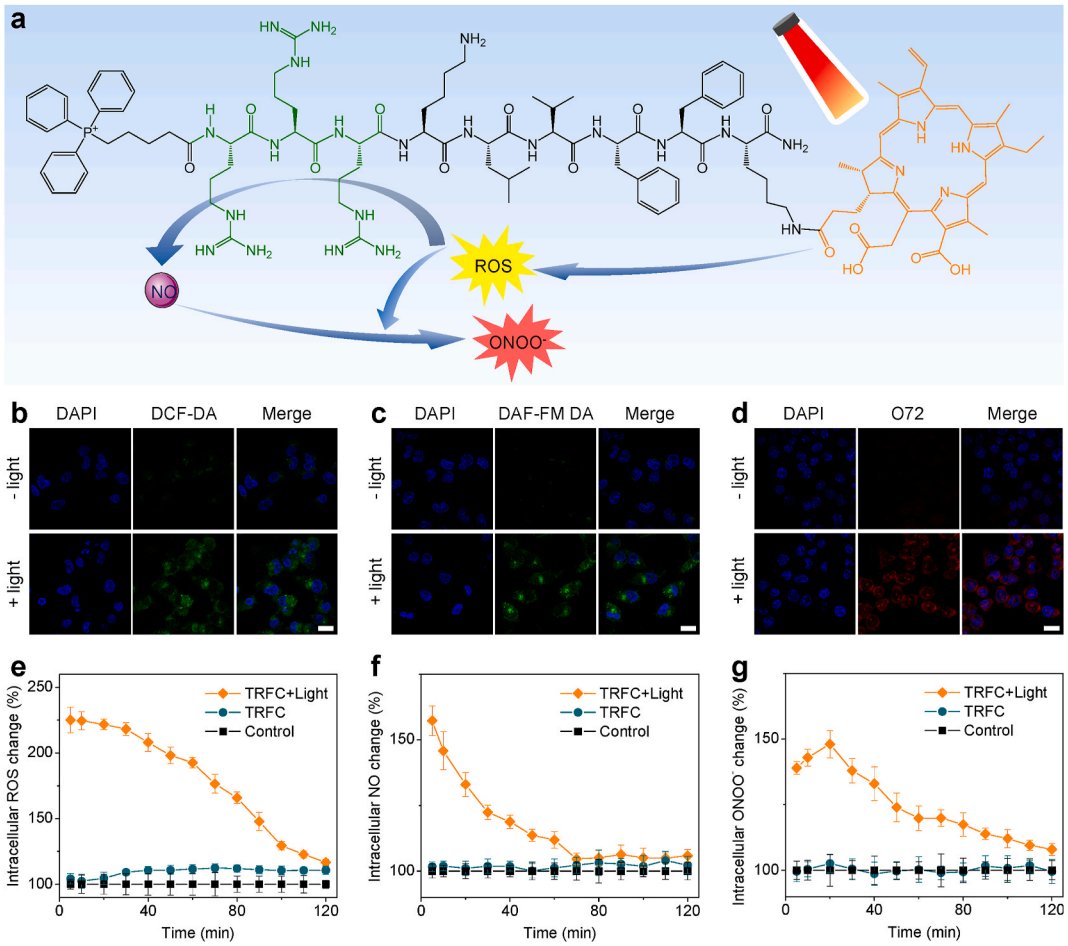

Fig. 3. (a) Schematic illustration of light-triggered cascade reactions involving ROS, NO and $ONOO^-$ generation. Confocal images of ROS (b), NO (c) and $ONOO^-$ (d) generation in 4T1 cells after incubation with TRFC NPs followed with or without light irradiation (660 nm, 0.25 W cm^{-2}, 3 min). Scale bar: 20 μm. The influence of TRFC NPs on intracellular ROS (e), NO (f) and $ONOO^-$ (g) levels in 4T1 cells with or without light irradiation (660 nm, 0.25 W cm^{-2}, 3 min).

had a relatively high accumulation in liver owing to the uptake by the mononuclear phagocyte system (MPS) in liver just as many other nanomedicines [40].

3.3. Intracellular ROS, NO and $ONOO^-$ determination

As aforementioned, TRFC NPs underwent a cascade reaction to fulfill the structural transformation behavior. When triggered by light, the photosensitizer Ce6 generated ROS, and subsequently oxidized the oligoarginine to produce NO gas, followed by the production of $ONOO^-$ (Fig. 3a). In order to investigate the ROS, NO and $ONOO^-$ production in living cells, corresponding fluorescent probes were employed to stain cells and observed using CLSM. 2′,7′-dichlorofluorescein diacetate (DCF-DA), as a ROS fluorescent probe, was employed to observe the intracellular ROS production. From Fig. 3b, after incubation with TRFC NPs, 4T1 cells showed obvious green fluorescence upon exposure to light irradiation, indicating the successful generation of abundant ROS in cells. Similarly, 4-amino-5-methylamino-2′,7′-dichlorofluorescein diacetate (DAF-FM DA), as a NO fluorescent probe, was applied to visualize the intracellular NO production. From Figs. 3c and 4T1 cells also showed clear green fluorescence after incubation with TRFC NPs and exposure to light irradiation, demonstrating the successful generation of NO in cells. NO can react with ROS to yield $ONOO^-$, which is the critical product that can aggravate the total damage to cancer cells. After confirmation of the ROS and NO generation, the intracellular $ONOO^-$ was further investigated by using a fluorescent probe, BBoxiProbe® O72, which could be specifically oxidized by $ONOO^-$ and emit red fluorescence. As displayed in Fig. 3d, an intensive red fluorescence was detected in the cells treated by TRFC NPs plus light irradiation, proving the successful generation of $ONOO^-$. By contrast, both green fluorescence and red fluorescence were hardly observed in cells in the absence of light irradiation. The generation of NO and $ONOO^-$ enabled to greatly improve the PDT efficacy owing to the longer diffusion distance of NO and more potent cytotoxicity of $ONOO^-$ in comparison to ROS. In addition to the qualitative observation by CLSM, the intracellular changes of ROS, NO and $ONOO^-$ levels were further determined by using a microplate reader. As shown in Fig. 3e and Fig. S12 (Supporting Information), the ROS levels in 4T1 cells treated by TRFC NPs were particle concentration dependent, and increased dramatically upon exposure to light irradiation and then decreased gradually with time. The intracellular NO level also showed a similar change trend to ROS, which was reasonable as the NO generation was positive correlation with the ROS concentration (Fig. 3f). In terms of $ONOO^-$, the intracellular level was also particle concentration dependent (Fig. S13, Supporting Information). Upon exposed to light irradiation, the $ONOO^-$ level increased gradually at the beginning, which could be due to that the generation rate of $ONOO^-$ was

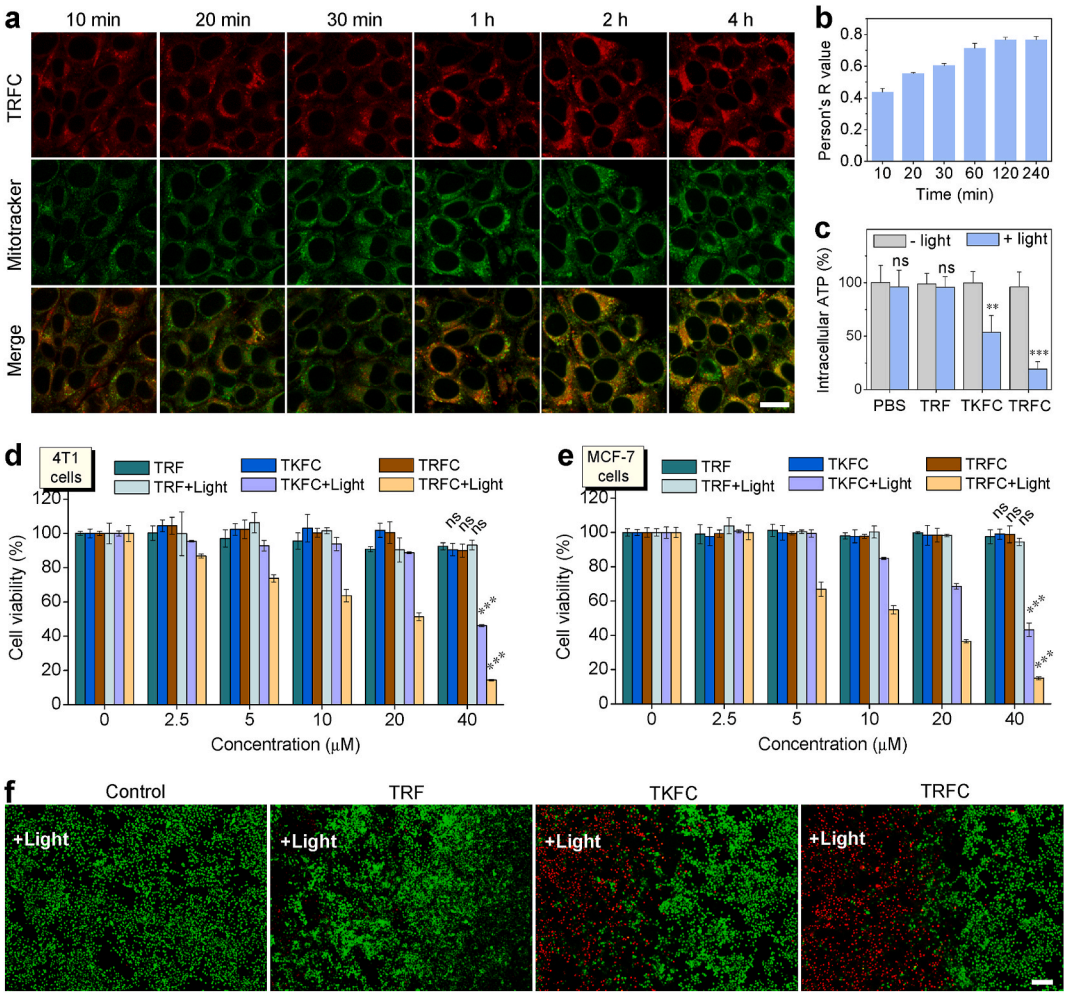

Fig. 4. (a) Representative CLSM images of the time-dependent colocalization of TRFC NPs with mitochondria in 4T1 cells. Scale bar: 20 μm. (b) Calculated Pearson correlation coefficient (Pearson's R) for colocalization analysis of images in (a). (c) Cell energy metabolism evaluation of intracellular ATP in 4T1 cells after incubation with TRF, TKFC and TRFC NPs, followed with or without light irradiation (660 nm, 0.25 W cm^{-2}, 3 min). *In vitro* cytotoxicity of different concentrations of TRF, TKFC, and TRFC NPs against 4T1 (d) and MCF-7 (e) cells with or without light irradiation (660 nm, 0.25 W cm^{-2}, 3 min). (f) LIVE/DEAD fluorescence images of 4T1 cells treated with TRF, TKFC and TRFC NPs, followed with or without light irradiation (660 nm, 0.25 W cm^{-2}, 3 min) and stained with Calcein-AM/PI. Scale bar, 200 μm. The data were presented as mean ± SD. *P* values were calculated by two-tailed Student's t-test (*$P < 0.05$; **$P < 0.01$; ***$P < 0.001$; ns, no significance).

faster than the depletion rate by cells. With the decrease of ROS and NO concentration, the generation rate of $ONOO^-$ became slower than the depletion rate, therefore the intracellular concentration decreased correspondingly (Fig. 3g).

3.4. Mitochondria targeting and in vitro anticancer activity

Given that mitochondria are the main energy source of cells and NO is able to induce the death of cancer cells by inhibiting their energy metabolism, the TRFC NPs were designed to target to mitochondria. In order to investigate the targeting efficiency of TRFC NPs to mitochondria, the colocalization degree between TRFC NPs and mitochondria was evaluated by CLSM. 4T1 cells were incubated with TRFC NPs for different time durations ranging from 10 min to 4 h. Subsequently, the cells were stained by MitoTracker and imaged by CLSM. As demonstrated in Fig. 4a–b, mitochondria (green) and TRFC NPs (red) started to colocalize within 10 min at a relatively low colocalization efficiency (Pearson's R value = 0.44). With the elongation of incubation time, the colocalization degree increased and achieved the maximum at around 2 h (Pearson's R value = 0.79), as indicated by the yellow color in the merged view. Similarly, the incubation of TRFC NPs with MCF-6 and B16 cells also revealed a high mitochondrial targeting ability, with Pearson's R value higher than 0.8 (Fig. S14, Supporting Information). These results jointly demonstrated that TRFC NPs could be taken up quickly by living cells and efficiently targeted to mitochondria. After verification of the subcellular localization of TRFC NPs, the intracellular ATP levels of living cells after incubation with TRFC NPs followed with or without light irradiation were determined. From Fig. 4c, after irradiation by light, the intracellular ATP level in TRFC NPs treated group decreased dramatically to around 19%, which was significantly lower than that in cells treated by TKFC NPs (54%) and TRF NPs (96%). This difference possibly resulted from the NO generation triggered by light, which synergized with ROS and inhibited the energy metabolism of cancer cells. By contrast, in the absence of light irradiation, the intracellular ATP levels showed no difference from that in the control group. After the intracellular ATP measurement, a CCK-8 assay was implemented to evaluate the cytotoxicity of TRF, TKFC and TRFC NPs on 4T1, MCF-7 and B16 cells. The cells were treated with a series of concentrations of NPs. As demonstrated in Fig. 4d–e and Fig. S15–S18 (Supporting Information), in the absence of light irradiation, TRF, TKFC and TRFC NPs showed a little cytotoxicity to cancer cells, indicating low dark cytotoxicity of the designed materials. Under light irradiation, TRF, TKFC and TRFC NPs showed a remarkably increased cytotoxicity to cancer cells in a dose-dependent manner. Notably, TRFC NPs displayed significantly higher cancer cell-killing efficiency than TKFC NPs, probably owing to the generation of NO and $ONOO^-$ from TRFC NPs. LIVE/DEAD assay was implemented to further visualize the NO enhanced PDT efficacy. The living cells and dead cells were stained with Calcein AM (green) and PI (red), respectively. As revealed from Fig. 4f, TRFC NPs were more efficient than TKFC NPs to cause remarkable cytotoxicity to cancer cells under light irradiation (660 nm, 0.25 W cm^{-2}, 3 min), which were in good consistence with the results of CCK-8 assay. In addition, the Annexin V-FITC/PI staining assay was executed to investigate the *in vitro* apoptosis-inducing capacity of TRF, TKFC and TRFC NPs by flow cytometry. As shown in Fig. S19 (Supporting Information), after light irradiation (660 nm, 0.25 W cm^{-2}, 3 min) and short incubation, TRFC NPs caused around 35% of the total apoptotic ratio to 4T1 cells, whereas the total apoptotic ratio induced by TKFC NPs was only about 19%. Without light treatment, TRF, TKFC and TRFC NPs did not show pro-apoptotic effects. All the above experimental results confirmed the practicability and therapeutic effectiveness of NO sensitized PDT treatment.

3.5. In vivo antitumor effect

Encouraged by the good *in vitro* cancer cell-killing results of TRFC NPs, the *in vivo* antitumor effect of TRFC NPs was further evaluated using a 4T1 tumor-bearing mice model. In order to avoid non-specific tissue damage, a treatment strategy of multi-time light irradiation with a low power density (0.25 W cm^{-2}, 660 nm) and a short time duration (3 min) was adopted. All the tumor-bearing mice were randomly assigned into eight groups, and were treated according to the schedule shown in Fig. 5a. PBS, TRF NPs, TKFC NPs and TRFC NPs were intravenously injected into mice *via* the tail vein (designated as Day 0), respectively. Based on the above-mentioned results that light irradiation can induce the structural transformation of TRFC NPs and enhance the intratumoral retention and accumulation of NPs, the first light irradiation was conducted at 4 h post-injection to trigger the structural transformation for enhanced intratumoral retention and accumulation. The second light irradiation was performed at 6 h post-injection, corresponding to the time with maximum accumulation level, for therapy. The third light irradiation was implemented at 24 h post-injection to make full use of the retained nanomedicines in tumors for therapy. Therefore, one course of treatment included one time of injection and three times of light irradiation. From Fig. 5b–d, compared with PBS groups, the TRF, TKFC and TRFC NPs did not display any visible tumor inhibition effects in the absence of light irradiation. The PBS plus light irradiation group showed negligible difference from the other groups without light treatment, implying that the light dose had no effects on tumor growth. In the presence of light irradiation, the TKFC NPs displayed a gentle effect on the inhibition of tumor growth, and the TRFC NPs showed a significant tumor suppression effect, especially within 6 days after intravenous injection. From Day 7, it seemed that tumors tended to increase, and therefore a second course of treatment was carried out from Day 9. Notably, after the second course of treatment, the TKFC NPs plus light irradiation showed limited tumor suppression effect, indicating that PDT alone was insufficient to suppress tumor growth in the present conditions. By contrast, the TRFC NPs showed an exhaustive inhibition capability after light irradiation among all the treatment groups, which probably resulted from the structural transformation enhanced intratumoral retention as well as the NO amplified PDT efficacy owing to the generation of NO gas with free diffusion capacity and $ONOO^-$ with remarkably increased cytotoxicity. In order to better understand the excellent therapeutic efficacy of TRFC NPs to tumors, the intratumoral $ONOO^-$ and NO levels after light irradiation at 4 h and 6 h post-injection of TRFC NPs were determined using DAF-FM DA and BBoxiProbe® O72 probes, respectively. The results demonstrated that compared with the tumors without light irradiation, the intratumoral $ONOO^-$ level with light irradiation at 4 h increased remarkably. More importantly, after the second light irradiation at 6 h, the $ONOO^-$ level further increased dramatically (Fig. 5e). Similarly, a significant increase of intratumoral NO level was also observed after light irradiation at 4 h and 6 h post-injection of TRFC NPs (Fig. S20, Supporting Information). These results explained the exhaustive inhibition capability of TRFC NPs when irradiated by light. The effective NO sensitized PDT treatment was further confirmed by post-mortem histological analysis. As demonstrated from the H&E staining results (Fig. 5f), the TRFC NPs plus light irradiation group displayed remarkably reduced cell density and damaged structure of cancer cells. The TKFC NPs plus irradiation group displayed a moderate degree of decrease in cell density. In contrast, densely packed neoplastic cells were observed in other groups, manifesting no distinct cell death occurred in these groups, which were in good consistence with the treatment results above.

Moreover, we further investigated the influence of NO gas enhanced PDT on tumor microenvironment (TME) to gain a better insight of its therapeutic mechanism on tumor therapy. TME involves various tumor-associated stromal cells, including inflammatory cells, vascular cells, and fibroblasts, which are all closely associated with tumor proliferation, metastasis, angiogenesis, and immune suppression. Therefore, the destruction of TME is of equal importance with directly killing tumor cells to achieve a complete eradication of tumor and avoid its reoccurrence. In current work, immunofluorescence analysis including Ki67

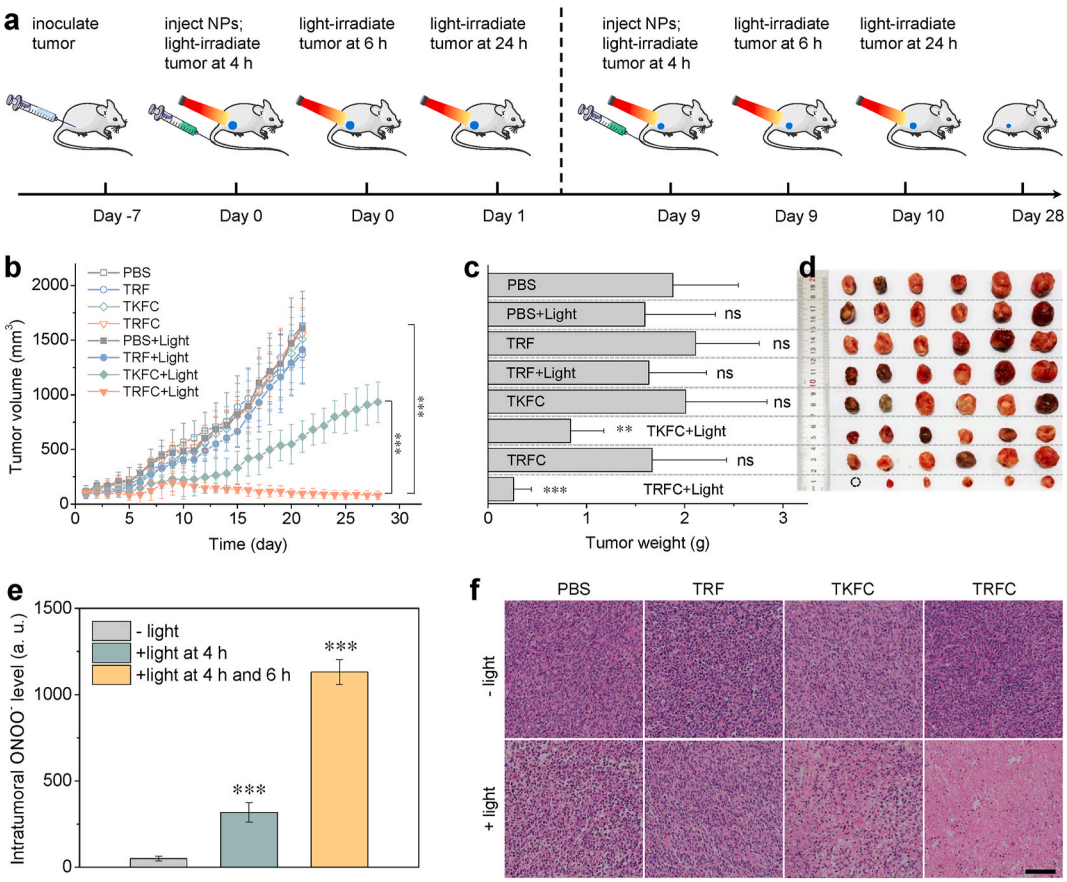

Fig. 5. *In vivo* anti-tumor efficacy. (a) Schematic illustration of establishing the subcutaneous 4T1 tumor model and *in vivo* therapeutic schedule. (b) Tumor growth inhibition curves of mice receiving the indicated treatments. (c) Tumor weight comparison after treatments, and (d) corresponding digital images of excised tumors from mice at the end of treatments ($n = 6$). The small circle indicated that the tumor disappeared in that mouse. (e) Intratumoral $ONOO^-$ level measurements with or without light irradiation (660 nm, 0.25 W cm^{-2}, 3 min). (f) Representative images of tumor slices after H&E staining (scale bar, 100 μm). The data were presented as mean ± SD. *P* values were calculated by two-tailed Student's t-test (*$P < 0.05$; **$P < 0.01$; ***$P < 0.001$; ns, no significance).

staining, terminal deoxynucleotidyl transferase-mediated dUTP nick end labeling (TUNEL) staining, Iba1 staining, and CD31 staining were performed to evaluate the change of TME. As revealed in Fig. 6 and Fig. S21 (Supporting Information), after the treatment, the expression level of Ki67 in tumor tissue was significantly reduced in the TRFC + light group. Additionally, TUNEL staining results demonstrated remarkable increase of red fluorescence in the TRFC + light group, indicating severe apoptosis of tumor cells. Moreover, the Iba1 staining displayed the full eradication of tumor-associated macrophages, and the CD31 staining showed a dramatic regression of vasculatures in tumor, suggesting that the whole TME was altered in the TRFC + light group. By contrast, other groups did not induce such significant changes on TME. The demilitarization of tumor-induced immunodepression well explained the excellent therapeutic outcome of NO sensitized PDT. All these results demonstrated that the designed TRFC NPs were able to amplify PDT efficacy. On the other hand, it is worth noting that given the limited tissue penetration depth of light, the developed TRFC NPs are only suitable for the treatment of superficial tumor. In order for better clinical applications, the developed NPs can be further engineered to respond to other stimulus including X-ray irradiation, ultrasound or magnetism.

Due to the distribution of NPs in main organs after intravenous injection, the biosafety of TRFC NPs was evaluated. As shown in Fig. S22–S23 (Supporting Information), neither distinct body weight change nor visible damage to main organs (heart, liver, spleen, lung, and kidney) after treatment was observed in all treatment groups, suggesting good tissue compatibility of the TRFC NPs. Furthermore, to evaluate clinical translation potential of TRFC NPs, a detailed examination of *in vivo* toxicology was implemented. The standard blood biochemical indexes (alkaline phosphatase ALP, alanine transaminase ALT, aspartate transaminase AST, creatinine CREA and blood urea nitrogen BUN) and general haematology parameters (white blood cells WBC, red blood cells RBC, haemoglobin HGB, mean corpuscular haemoglobin concentration MCHC, lymphocyte LYM, haematocrit HCT, mean corpuscular volume MCV, mean corpuscular haemoglobin MCH, and red blood cell distribution width-standard deviation RDW-SD) were analyzed after intravenous administration of a series of concentrations of the TRFC NPs (10, 20, 40, 80 mg kg^{-1}) and then the blood was collected from mice orbit after one week. The blood biochemical indexes and haematology parameters of mice after intravenous injection of TRFC NPs showed no statistically significant difference from that in the control group (Fig. S24–S25, Supporting Information), indicating no obvious toxicity to liver and kidney and excellent blood compatibility.

4. Conclusion

In this study, we reported an innovative mitochondria-targeting chimeric peptide that can self-assemble into nanospheres and transform into nanorods upon irradiated by light, in support of enhanced intratumoral retention. The sphere–to–rod structural transformation was realized *via* a cascade reaction involving the generation of ROS induced by light and the subsequent release of NO gas. More importantly, the designed TRFC NPs were able to amplify PDT efficacy *via* the generation of $ONOO^-$ with remarkably increased cytotoxicity. Lack of either Ce6 domain or NO donor domain resulted in the loss of nanorod transformation property and decreased anti-tumor activity. TRFC NPs

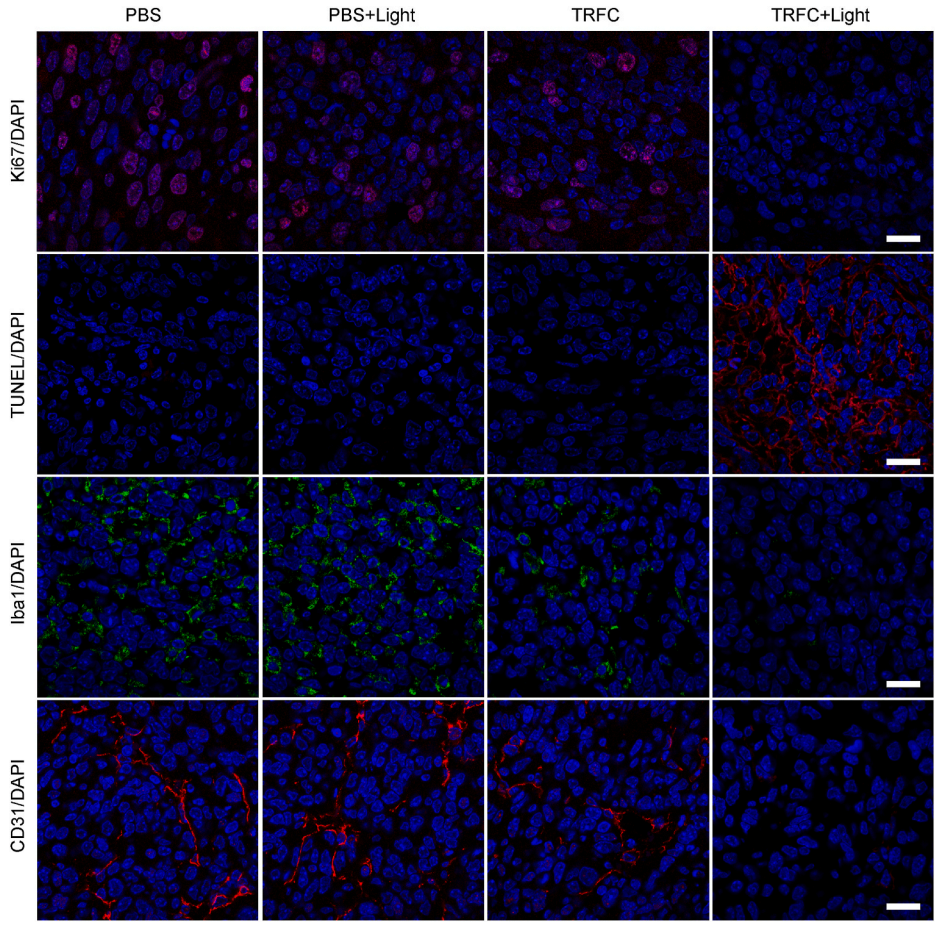

Fig. 6. Immunohistochemical analysis of Ki67^{+} proliferating cells, TUNEL^{+} apoptotic cells, Iba1^{+} tumor-associated macrophages and CD31^{+} tumor vessels in 4T1 tumors with different treatments. Scale bar: 20 μm.

represented an innovated paradigm enabling sphere−to−rod structural transformation only by easy manipulation of light. The light-mediated transformation strategy provides a promising prospect for enhanced intratumoral accumulation of therapeutic agents and improved therapeutic outcomes.

CRediT authorship contribution statement

Lingdong Jiang: conceived the project idea, conducted the experiments, Formal analysis, Writing – original draft. **Danyang Chen:** provided suggestions for experiments and helped with some of the experiments. **Zhaokui Jin:** provided suggestions for experiments. **Chao Xia:** provided suggestions for experiments. **Qingqing Xu:** helped with some of the experiments. **Mingjian Fan:** helped with some of the experiments. **Yunlu Dai:** Funding acquisition, provided funding and suggestions for the manuscript. **Jia Liu:** helped with some of the experiments and provided suggestions for the manuscript. **Yuanpei Li:** helped in planning the project and provided suggestions for the manuscript. **Qianjun He:** conceived the project idea, Formal analysis, Writing – original draft, Supervision.

Declaration of competing interest

The authors declare no conflicts of interest regarding the publication of this paper.

Acknowledgments

We greatly appreciate the Instrumental Analysis Center of Shenzhen University (Lihu campus) for assistance in material characterizations. This work was financially supported by National Natural Science Foundation of China (51872188), Shenzhen Basic Research Program (SGDX20201103093600004), Special Funds for the Development of Strategic Emerging Industries in Shenzhen (20180309154519685), SZU Top Ranking Project (860-00000210), Basic and Applied Basic Research Foundation of Guangdong Province (2019A1515110294), and the Postdoctoral Science Foundation of China (2020M672798).

Appendix A. Supplementary data

Supplementary data to this article can be found online at https://doi.org/10.1016/j.bioactmat.2021.09.035.

References

[1] H. Maeda, Toward a full understanding of the EPR effect in primary and metastatic tumors as well as issues related to its heterogeneity, Adv. Drug Deliv. Rev. 91 (2015) 3–6.
[2] S. Wilhelm, A.J. Tavares, Q. Dai, S. Ohta, J. Audet, H.F. Dvorak, W.C.W. Chan, Analysis of nanoparticle delivery to tumours, Nat. Rev. Mater. 1 (2016) 16014.
[3] C.-H. Heldin, K. Rubin, K. Pietras, A. Östman, High interstitial fluid pressure — an obstacle in cancer therapy, Nat. Rev. Cancer 4 (2004) 806–813.
[4] C.S. Kue, A. Kamkaew, K. Burgess, L.V. Kiew, L.Y. Chung, H.B. Lee, Small molecules for active targeting in cancer, Med. Res. Rev. 36 (2016) 494–575.
[5] N. Bertrand, J. Wu, X. Xu, N. Kamaly, O.C. Farokhzad, Cancer nanotechnology: the impact of passive and active targeting in the era of modern cancer biology, Adv. Drug Deliv. Rev. 66 (2014) 2–25.
[6] U. Prabhakar, H. Maeda, R.K. Jain, E.M. Sevick-Muraca, W. Zamboni, O. C. Farokhzad, S.T. Barry, A. Gabizon, P. Grodzinski, D.C. Blakey, Challenges and key considerations of the enhanced permeability and retention effect for nanomedicine drug delivery in oncology, Cancer Res. 73 (2013) 2412–2417.

[7] D. Li, Z. Tang, Y. Gao, H. Sun, S. Zhou, A bio-inspired rod-shaped nanoplatform for strongly infecting tumor cells and enhancing the delivery efficiency of anticancer drugs, Adv. Funct. Mater. 26 (2016) 66–79.

[8] H. Cabral, Y. Matsumoto, K. Mizuno, Q. Chen, M. Murakami, M. Kimura, Y. Terada, M.R. Kano, K. Miyazono, M. Uesaka, N. Nishiyama, K. Kataoka, Accumulation of sub-100 nm polymeric micelles in poorly permeable tumours depends on size, Nat. Nanotechnol. 6 (2011) 815–823.

[9] L. Xu, Y. Wang, C. Zhu, S. Ren, Y. Shao, L. Wu, W. Li, X. Jia, R. Hu, R. Chen, Z. Chen, Morphological transformation enhances tumor retention by regulating the self-assembly of doxorubicin-peptide conjugates, Theranostics 10 (2020) 8162–8178.

[10] R. Liu, M. Yu, X. Yang, C.S. Umeshappa, C. Hu, W. Yu, L. Qin, Y. Huang, H. Gao, Linear chimeric triblock molecules self-assembled micelles with controllably transformable property to enhance tumor retention for chemo-photodynamic therapy of breast cancer, Adv. Funct. Mater. 29 (2019) 1808462.

[11] Y. Zhang, F. Huang, C. Ren, J. Liu, L. Yang, S. Chen, J. Chang, C. Yang, W. Wang, C. Zhang, Q. Liu, X. Liang, J. Liu, Enhanced radiosensitization by gold nanoparticles with acid-triggered aggregation in cancer radiotherapy, Adv. Sci. 6 (2019) 1801806.

[12] K. Han, J. Zhang, W. Zhang, S. Wang, L. Xu, C. Zhang, X. Zhang, H. Han, Tumor-triggered geometrical shape switch of chimeric peptide for enhanced *in vivo* tumor internalization and photodynamic therapy, ACS Nano 11 (2017) 3178–3188.

[13] Z. Qin, T. Du, Y. Zheng, P. Luo, J. Zhang, M. Xie, Y. Zhang, Y. Du, L. Yin, D. Cui, Q. Lu, M. Lu, X. Wang, H. Jiang, Glutathione induced transformation of partially hollow gold–silver nanocages for cancer diagnosis and photothermal therapy, Small 15 (2019) 1902755.

[14] D.-B. Cheng, D. Wang, Y.-J. Gao, L. Wang, Z.-Y. Qiao, H. Wang, Autocatalytic morphology transformation platform for targeted drug accumulation, J. Am. Chem. Soc. 141 (2019) 4406–4411.

[15] L. Zhang, D. Jing, N. Jiang, T. Rojalin, C.M. Baehr, D. Zhang, W. Xiao, Y. Wu, Z. Cong, J.J. Li, Y. Li, L. Wang, K.S. Lam, Transformable peptide nanoparticles arrest HER2 signalling and cause cancer cell death *in vivo*, Nat. Nanotechnol. 15 (2020) 145–153.

[16] W. Fan, P. Huang, X. Chen, Overcoming the Achilles' heel of photodynamic therapy, Chem. Soc. Rev. 45 (2016) 6488–6519.

[17] C. Pan, M. Ou, Q. Cheng, Y. Zhou, Y. Yu, Z. Li, F. Zhang, D. Xia, L. Mei, X. Ji, Z-scheme heterojunction functionalized pyrite nanosheets for modulating tumor microenvironment and strengthening photo/chemodynamic therapeutic effects, Adv. Funct. Mater. 30 (2020) 1906466.

[18] W. Zeng, H. Zhang, Y. Deng, A. Jiang, X. Bao, M. Guo, Z. Li, M. Wu, X. Ji, X. Zeng, L. Mei, Dual-response oxygen-generating MnO_2 nanoparticles with polydopamine modification for combined photothermal-photodynamic therapy, Chem. Eng. J. 389 (2020) 124494.

[19] H. Chen, X. Zeng, H.P. Tham, S.Z.F. Phua, W. Cheng, W. Zeng, H. Shi, L. Mei, Y. Zhao, NIR-light-activated combination therapy with a precise ratio of photosensitizer and prodrug using a host–guest strategy, Angew. Chem. Int. Ed. 58 (2019) 7641–7646.

[20] W.A. Pryor, Oxy-radicals and related species: their formation, lifetimes, and reactions, Annu. Rev. Physiol. 48 (1986) 657–667.

[21] S. Hatz, J.D.C. Lambert, P.R. Ogilby, Measuring the lifetime of singlet oxygen in a single cell: addressing the issue of cell viability, Photochem. Photobiol. Sci. 6 (2007) 1106.

[22] R.F. Furchgott, Endothelium-derived relaxing factor: discovery, early studies, and identification as nitric oxide (Nobel Lecture), Angew. Chem. Int. Ed. Engl. 38 (1999) 1870–1880.

[23] C. Szabo, Gasotransmitters in cancer: from pathophysiology to experimental therapy, Nat. Rev. Drug Discov. 15 (2016) 185–203.

[24] D. Chen, Z. Jin, B. Zhao, Y. Wang, Q. He, MBene as a theranostic nanoplatform for photocontrolled intratumoral retention and drug release, Adv. Mater. 33 (2021) 2008089.

[25] T. Luo, D. Wang, L. Liu, Y. Zhang, C. Han, Y. Xie, Y. Liu, J. Liang, G. Qiu, H. Li, D. Su, J. Liu, K. Zhang, Switching reactive oxygen species into reactive nitrogen species by photocleaved O_2-released nanoplatforms favors hypoxic tumor repression, Adv. Sci. (2021) 2101065.

[26] Q. Li, J. Zhang, J. Li, H. Ye, M. Li, W. Hou, H. Li, Z. Wang, Glutathione-activated NO-/ROS-generation nanoparticles to modulate the tumor hypoxic microenvironment for enhancing the effect of HIFU-combined chemotherapy, ACS Appl. Mater. Interfaces 13 (2021) 26808–26823.

[27] S.-S. Wan, J.-Y. Zeng, H. Cheng, X.-Z. Zhang, ROS-induced NO generation for gas therapy and sensitizing photodynamic therapy of tumor, Biomaterials 185 (2018) 51–62.

[28] Z. Yuan, C. Lin, Y. He, B. Tao, M. Chen, J. Zhang, P. Liu, K. Cai, Near-infrared light-triggered nitric-oxide-enhanced photodynamic therapy and low-temperature photothermal therapy for biofilm elimination, ACS Nano 14 (2020) 3546–3562.

[29] P.G. Wang, M. Xian, X. Tang, X. Wu, Z. Wen, T. Cai, A.J. Janczuk, Nitric oxide donors: chemical activities and biological applications, Chem. Rev. 102 (2002) 1091–1134.

[30] K. Zhang, H. Xu, X. Jia, Y. Chen, M. Ma, L. Sun, H. Chen, Ultrasound-triggered nitric oxide release platform based on energy transformation for targeted inhibition of pancreatic tumor, ACS Nano 10 (2016) 10816–10828.

[31] S. Moncada, J.D. Erusalimsky, Does nitric oxide modulate mitochondrial energy generation and apoptosis? Nat. Rev. Mol. Cell Biol. 3 (2002) 214–220.

[32] V. Borutaité, G.C. Brown, Rapid reduction of nitric oxide by mitochondria, and reversible inhibition of mitochondrial respiration by nitric oxide, Biochem. J. 315 (1996) 295–299.

[33] I. Coin, M. Beyermann, M. Bienert, Solid-phase peptide synthesis: from standard procedures to the synthesis of difficult sequences, Nat. Protoc. 2 (2007) 3247–3256.

[34] P.-P. Yang, Q. Luo, G.-B. Qi, Y.-J. Gao, B.-N. Li, J.-P. Zhang, L. Wang, H. Wang, Host materials transformable in tumor microenvironment for homing theranostics, Adv. Mater. 29 (2017) 1605869.

[35] J. Meng, Z. Jin, P. Zhao, B. Zhao, M. Fan, Q. He, A multistage assembly/disassembly strategy for tumor-targeted CO delivery, Sci. Adv. 6 (2020), eaba1362.

[36] C. Szabó, H. Ischiropoulos, R. Radi, Peroxynitrite: biochemistry, pathophysiology and development of therapeutics, Nat. Rev. Drug Discov. 6 (2007) 662–680.

[37] D. Jiang, T. Yue, G. Wang, C. Wang, C. Chen, H. Cao, Y. Gao, Peroxynitrite ($ONOO^-$) generation from the HA-TPP@NORM nanoparticles based on synergistic interactions between nitric oxide and photodynamic therapies for elevating anticancer efficiency, New J. Chem. 44 (2020) 162–170.

[38] Y. Deng, F. Jia, S. Chen, Z. Shen, Q. Jin, G. Fu, J. Ji, Nitric oxide as an all-rounder for enhanced photodynamic therapy: hypoxia relief, glutathione depletion and reactive nitrogen species generation, Biomaterials 187 (2018) 55–65.

[39] Z. Zhang, H. Yan, S. Li, Y. Liu, P. Ran, W. Chen, X. Li, Janus rod-like micromotors to promote the tumor accumulation and cell internalization of therapeutic agents, Chem. Eng. J. 404 (2021) 127073.

[40] Y. Zhou, Z. Dai, New strategies in the design of nanomedicines to oppose uptake by the mononuclear phagocyte system and enhance cancer therapeutic efficacy, Chem. Asian J. 13 (2018) 3333–3340.